# Improvement of the performance and accuracy of PET Monte Carlo simulations

Habib Zaidi[†,*], Claire Labbé, and Christian Morel

Division of Nuclear Medicine, Geneva University Hospital, CH-1211 Geneva 4, SWITZERLAND

## ABSTRACT

The many applications of Monte Carlo modelling in PET arouse to increase the accuracy and computational speed of Monte Carlo codes. The accuracy of Monte Carlo simulations strongly depends on cross-section libraries used for photon transport calculations. Furthermore, large amounts of CPU time are required to obtain meaningful simulated data. We present a comparison of different photon cross-section libraries together with the parallel implementation of the 3D PET Monte Carlo simulator, *Eidolon* on a MIMD parallel architecture. Different photon cross-section libraries and parametrizations show quite large variations as compared to the most recent EPDL97 nuclear data files for energies from 1 keV to 1 MeV. Together with the optimisation of the computing time performances of the Monte Carlo software, photon transport in 3D PET could be efficiently modelled to better understand scatter correction techniques. In implementing *Eidolon* on a parallel platform, a linear speedup factor was achieved with the number of computing nodes.

**Keywords:** Photon cross-section library, Monte Carlo, PET, parallel computing.

## 1. INTRODUCTION

The Monte Carlo method is widely used for solving problems involving statistical processes and is very useful in nuclear medical imaging due to the stochastic nature of radiation emission, transport and detection processes. The method is very useful for complex problems that cannot be modelled by computer codes using deterministic methods or when experimental measurements may be impractical. In particular, Monte Carlo modelling allows a detailed investigation of the spatial and energy distribution of Compton scatter which would be difficult to perform using present experimental techniques, even with very good energy resolution detectors. The lack of inherent error estimates and relatively slow convergence is a well known limitation of the Monte Carlo technique.[1] Accurate Monte Carlo simulations rely on detailed understanding and modelling of radiation transport and on the availability of reliable, physically-consistent databases.[2] The Lawrence Livermore National Laboratory (LLNL) houses the world's most extensive nuclear and atomic cross-section database, which parametrizes the interactions of photons, electrons/positrons, neutrons, protons, and other heavy charged particles. A key feature of the LLNL database is that it is the only exhaustive interaction cross-section compilation available. A comparison between an up-to-date source of cross-section data developed by LLNL (EPDL97[3]) with other more familiar photon interaction databases (XCOM[4] and PHOTX[5]) and parametrizations implemented in public domain simulation packages (GEANT[6] and PETSIM[7]) in interval from 1 to 1000 keV was performed for some human tissues and detector materials of interest in Positron Emission Tomography (PET) imaging.

Since Monte Carlo calculations are extremely time-consuming, the development of advanced computers with special capabilities for vectorized or parallel calculations opened a new way for Monte Carlo researchers. Historically, most programs and software libraries have been developed to run on serial, single-processor computers. Nevertheless, it is worth pointing out that among all simulation techniques of physical processes, the Monte Carlo method is probably the most suitable one for parallel computing since the results of photon histories are completely independent from each other. A modification or adaptation of the code, however, is a prerequisite to run it on parallel computers. During the last two decades, investigations were carried out to run different Monte Carlo codes on multiple-transputer systems[8], vector parallel supercomputers[9], parallel computers[10] and a cluster of workstations in a local area network using Parallel Virtual Machine (PVM).[11]

## 2. PHOTON CROSS-SECTION LIBRARIES AND PARAMETRIZATIONS

For the energies of interest in nuclear imaging (below 1 MeV), when a photon passes through matter, any of the three interaction processes (photoelectric, incoherent scattering, coherent scattering) may occur. Every cross-section is peculiar to the type and energy of the incident particle and to the kind of interaction it undergoes. These partial cross-sections are summed to form the total cross-section; the ratio of the partial cross-section to the total cross-section gives the probability of this particular interaction occurring. The probability of a photon with a given energy $E$ undergoing absorption or scattering when crossing a layer of material $Z$ can be expressed quantitatively in terms of a linear attenuation coefficient $\mu$ (cm$^{-1}$) which is dependent on the material's density, $\rho$ (g/cm$^3$):[2]

$$\mu = \mu_{photo} + \mu_{incoh} + \mu_{coh} . \tag{1}$$

It is common to neglect coherent scattering in PET Monte Carlo simulation of photon transport because of its low contribution to the total cross-section at 511 keV. In order to justify some of the approximations made in Monte Carlo codes, the relative importance of the various processes involved in the energy range below 1 MeV were considered for some compounds and mixtures of interest in nuclear medicine. Figure 1 illustrates the relative strengths of the photon interactions versus energy for water and bismuth germanate, respectively. For water, a moderately low-$Z$ material, we denote two distinct regions of single interaction dominance: a photoelectric domain below 20 keV and an incoherent scattering domain above 20 keV. The coherent scattering contribution to the total cross-section is less than 1% for energies above 250 keV, justifying some of the approximations discussed above. However, this contribution is in the order of 7% for high-$Z$ materials like BGO. Therefore, efforts should be made to treat the coherent scattering process adequately for detector materials.

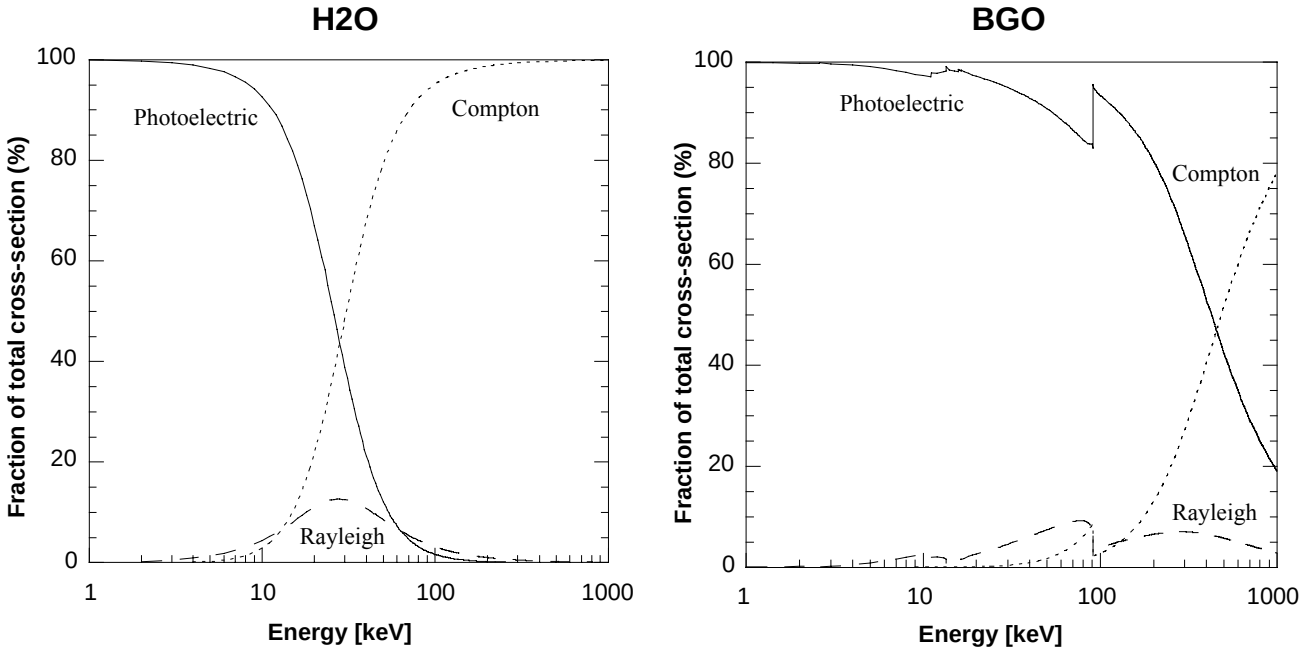


**Figure 1.** Components of photon cross-sections for water ($H_2O$) and bismuth germanate (BGO) showing the relative contribution and dominance region of each process.

Appropriate conversions between barns and (cm$^{-1}$) were made for each element. The macroscopic cross-section, $\sigma$ (cm$^{-1}$) for a compound or a mixture is given by:

$$\sigma = \rho N_a \sum_i \frac{w_i}{A_i} \sigma_i , \tag{2}$$

where $N_a$ is the Avogadro's number, $Z_i$ the atomic number of $i^{th}$ component of the medium, $A_i$ the atomic mass of $i^{th}$ component of the medium, $\rho$ the density of the medium, $w_i$ the fraction by weight of the $i^{th}$ component of the medium (values are from ICRU 44 report[12]), and $\sigma_i$ the atomic cross-section of the $i^{th}$ component of the medium.

For libraries where the mass attenuation coefficients $(\mu/\rho)_i$ are directly available for individual elements, the linear attenuation coefficients for mixtures and compounds are obtained according to:

$$\mu = \rho \sum_i w_i (\mu/\rho)_i . \tag{3}$$

### 2.1. XCOM

The compilation of XCOM[4] released on PC is available from The National Institute of Standards and Technology, through its Office of Standard Reference Data. It generates cross-sections and attenuation coefficients for all elements, compounds and mixtures as needed over a wide range of energies. To obtain $(\mu/\rho)_i$ values at every absorption edge for all constituent elements, interpolation were performed separately for the cross-sections indicated in Eq. (1), including the photoeffect cross-sections for the individual atomic subshells. This program was used to calculate the attenuation coefficients for the selected compounds presented in this paper.

### 2.2. PHOTX

The PHOTX[5] database from the National Bureau of Standards include interaction cross-sections and attenuation coefficients for 100 elements covering the energy range 1 keV to 100 GeV. The interactions considered are coherent and incoherent scatterings, photoelectric absorption, and pair production. A separate table gives the photo-effect cross-section for each electron shell. A linear interpolation routine was written to calculate coefficients between tabulated values in order to obtain a continuous set of cross-sections spanning energies from 1 to 1000 keV.

### 2.3. GEANT

The main applications of the GEANT[6] package are the transport of particles through an experimental set-up for the simulation of the detector responses with their graphical representations and the particle trajectories. Attenuation coefficients are parametrized through different routines within the software package.

#### 2.3.1 PHOTOELECTRIC EFFECT

Let $E$ be the incident gamma energy, and $\alpha = E/mc^2$. The photoelectric total cross-section per atom has been parametrized as:

$$\sigma(Z,\alpha) = \frac{Z^\beta}{\alpha^\gamma} F(Z,\alpha). \tag{4}$$

The parameters $\beta$ and $\gamma$ result from a fit, and F(Z,α) is defined as:

$$F(Z,\alpha) = \begin{cases} \left| \begin{array}{l} p_{1K}/Z + p_{2K}/\alpha + p_{3K} + p_{4K} Z + p_{5K}\alpha + p_{6K} Z^2 + p_{7K} Z\alpha + \\ p_{8K}\alpha^2 + p_{9K} Z^3 + p_{10K} Z^2\alpha + p_{11K} Z/\alpha^2 + p_{12K}\alpha^3 \end{array} \right| & \text{if } E > E_K \\ p_{1L1}/Z + p_{2L1}/\alpha + p_{3L1} & \text{if } E_{L1} < E \le E_K \\ p_{1L2}/Z + p_{2L2}/\alpha + p_{3L2} & \text{if } E_{L2} < E \le E_{L1} \\ p_{1M} & \text{if } 10\,keV \le E \le E_{L2} \end{cases} \tag{5}$$

The binding energy in the inner shells $E_i$ is parametrized as:

$$E_i(Z) = Z^2 \left(a_i + b_i Z + c_i Z^2 + d_i Z^3\right), \tag{6}$$

where $i$=$K$, $L_1$, $L_2$, and the constants $a_i$, $b_i$, $c_i$, and $d_i$ are tabulated inside dedicated functions.

The fit was made over 301 data points chosen between 5 ≤ Z ≤ 100 and 10 keV ≤ E ≤ 50 MeV.

#### 2.3.2. INCOHERENT SCATTERING

An empirical cross-section formula is used, which reproduces rather well the Compton scattering data down to 10 keV:

$$\sigma(Z,\alpha) = P_1(Z)\frac{\log(1+2\alpha)}{\alpha} + \frac{P_2(Z)+P_3(Z)\alpha+P_4(Z)\alpha^2}{1+a\alpha+b\alpha^2+c\alpha^3}, \tag{7}$$

where $P_i(Z) = Z\left(d_i + e_i Z + f_i Z^2\right)$

The fit was made over 511 data points chosen between $1 \le Z \le 100$ and 10 keV $\le E \le$ 100 GeV.

### 2.3.3. COHERENT SCATTERING

An empirical cross-section formula is used to reproduce the Rayleigh scattering data:

$$\sigma(Z,E) = aE^3 + bE^2 + cE + d\,. \tag{8}$$

For each element, the fit was obtained over 27 experimental values of the total coherent cross-section. The values of the coefficients are stored in a statement within the considered routine.

## 2.4. PETSIM

PETSIM has been developed to model both the source distributions and their attenuation characteristics, as well as septa and detectors used in PET.[7] In this code, the incoherent scattering linear attenuation coefficients are calculated by multiplying the electron density of the material by the total Compton scattering cross-sections, that is:

$$\sigma_{incoh} = \rho_e \; 2\pi r_o^2 \left\{ \frac{1+\alpha}{\alpha^2} \left| \frac{2(1+\alpha)}{(1+2\alpha)} - \frac{\ln(1+2\alpha)}{\alpha} \right| + \frac{\ln(1+2\alpha)}{2\alpha} - \frac{1+3\alpha}{(1+2\alpha)^2} \right. , \tag{9}$$

where $r_o$ is the classical electron radius and $\rho_e$ the electron density of the material (in electrons/cm$^3$) calculated using the relationship:

$$\rho_e = \rho \; N_a \sum_{i=1}^{n} \frac{w_i Z_i}{A_i}\,. \tag{10}$$

A linear log-log fitting was performed using the XCOM database on each side of the absorption edge to compute the 4 parameters required to calculate the photoelectric linear attenuation coefficient which is assumed to have the following form:

$$\tau = \begin{cases} A_1 E^{-B_1} & E > E_k \\ A_2 E^{-B_2} & E < E_k \end{cases}. \tag{11}$$

Table 1 shows relevant parameters for the selected materials studied in this paper.

**Table 1.** Parameters for the calculation of the linear attenuation coefficients for incoherent scattering and photoelectric absorption (Energy range: 15 to 511 keV).

| | **Incoherent scattering** | **Photoelectric absorption** | | | | |
|---|---|---|---|---|---|---|
| | Electron density $\rho_e$ | Fitting parameters above *K*-edge energy | | *K* absorption edge energy | Fitting parameters below *K*-edge energy | |
| **Material** | (electrons/cm$^3$) | $A_1$ | $B_1$ | (keV) | $A_2$ | $B_2$ |
| Air at NTP | $3.622 \infty 10^{20}$ | $7.680 \infty 10^{0}$ | 3.169 | <15 | - | - |
| Water | $3.343 \infty 10^{23}$ | $6.869 \infty 10^{3}$ | 3.192 | <15 | - | - |
| Lung, Inflated | $8.607 \infty 10^{22}$ | $1.799 \infty 10^{3}$ | 3.173 | <15 | - | - |
| Cortical bone | $5.950 \infty 10^{23}$ | $6.690 \infty 10^{4}$ | 3.071 | <15 | - | - |
| Brain | $3.438 \infty 10^{23}$ | $7.031 \infty 10^{3}$ | 3.171 | <15 | - | - |
| NaI(Tl) | $9.429 \infty 10^{23}$ | $1.999 \infty 10^{6}$ | 2.791 | 34 | $3.217 \infty 10^{5}$ | 2.791 |
| BGO | $1.806 \infty 10^{24}$ | $3.793 \infty 10^{6}$ | 2.584 | 95 | $9.942 \infty 10^{5}$ | 2.593 |
| $BaF_2$ | $1.243 \infty 10^{24}$ | $2.573 \infty 10^{6}$ | 2.771 | 40 | $4.456 \infty 10^{5}$ | 2.781 |
| LSO:Ce | $1.932 \infty 10^{24}$ | $4.545 \infty 10^{6}$ | 2.669 | 64 | $1.178 \infty 10^{6}$ | 2.736 |
| LuAP:Ce | $2.197 \infty 10^{24}$ | $4.699 \infty 10^{6}$ | 2.670 | 64 | $1.224 \infty 10^{6}$ | 2.737 |

### 2.5. THE EPDL97 LIBRARY

The Evaluated Photon Data Library (EPDL97) from Lawrence Livermore National Laboratory[3] includes photon interaction data for all elements with atomic number between $Z$ = 1 and 100 over the energy range 1 eV to 100 GeV, including photoionization, photoexcitation, coherent and incoherent scattering, and pair and triplet production cross-sections. Data files were truncated to match the needs of the diagnostic imaging community spanning energies from 1 keV to 1 MeV.[13] In addition to total interaction cross-sections, the cross-sections for photoelectric, incoherent and coherent scattering are also produced. The EPDL97 data include the effects of form factors and anomalous scattering factors in the incoherent coefficients, with the electron binding energies therefore contributing a noticeable influence on the shape of the incoherent coefficients.

## 3. COMPARATIVE EVALUATION

The most recent EPDL97 attenuation coefficients were compared for some human tissues (water, cortical bone, brain tissue, inflated lung and air) and detector materials (NaI(Tl), BGO, $BaF_2$, LSO:Ce and LuAP:Ce) of interest in PET imaging to earlier libraries (PHOTX, and XCOM), and parametrizations implemented in public domain simulation packages (GEANT, PETSIM) over the energy interval from 1 to 1000 keV. EPDL97 data points were given with 1 keV steps. The following example illustrates the difference between the cross-section libraries for water (Fig. 2). The coefficients appear to be qualitatively similar in this display format.

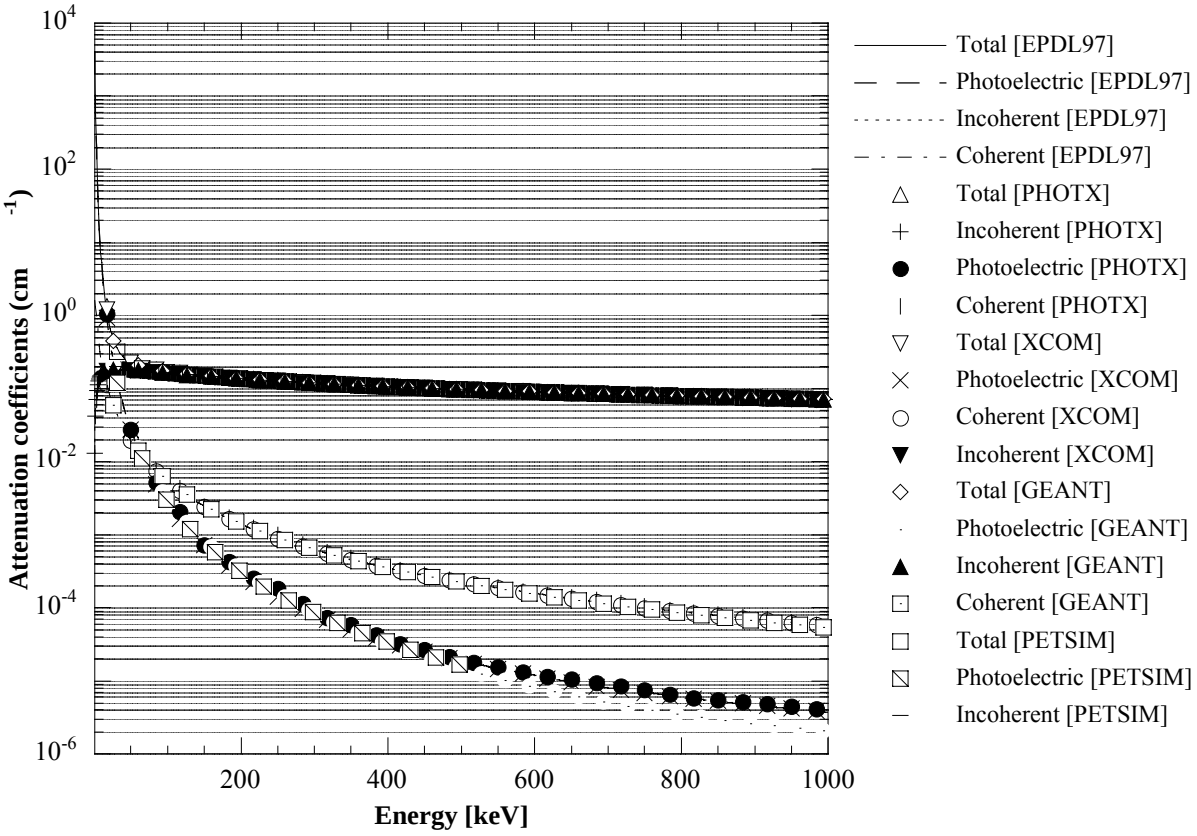


**Figure 2.** Comparison between different photon cross-section libraries and parametrizations for water ($H_2O$). The different processes contributing to the total linear attenuation coefficient are shown. The coefficients appear to be qualitatively similar in this display format.

In order to investigate differences between the EPDL97 database and the other libraries and parametrizations, percent differences between the individual coefficients are shown in figures 3 and 4 for water and NaI(Tl), respectively. The percent difference was calculated as $100 \times (\mu_c - \mu_{EPDL97}) / \mu_{EPDL97}$ , where $\mu_c$ is the coefficient being compared and $\mu_{EPDL97}$ are the EPDL97 coefficients.

The comparisons made in figures 3 and 4 are continuous and were calculated at 1 keV intervals between 1 and 1000 keV for both XCOM and PHOTX, between 10 and 1000 keV for GEANT, and between 15 and 511 keV for PETSIM. It is seen in that the differences can be as large as 25%. For PHOTX, the strong variations and oscillations visible in the plots as high frequency quasiperiodic noise is thought to be due to the discrete nature of the source data used and the crude interpolation used between the known coefficients which was chosen mainly to mimic the standard method used by most Monte Carlo developers. The parametric model used in PETSIM has an apparent problem in modelling the incoherent coefficients for low energies (<100 keV). This can be explained by the fact that XCOM uses a combination of the Klein-Nishina formula and non-relativistic Hartree-Fock incoherent scattering functions (which is about equal to 1 above 100 keV) to calculate the incoherent scattering, while only the Klein-Nishina relationship is used in PETSIM.[7] The discrepancy is even greater for high atomic number materials since the electrons can no longer be considered free. This should not however affect the accuracy of photon transport simulations within the phantoms since the low energy cut-off is generally higher than 200 keV.

The average positive difference between the GEANT and the EPDL97 coefficients for water are 0.3%, 9.61%, 0.31%, and 0.85%, for the total, photoelectric, incoherent and coherent attenuation coefficients, respectively. Larger differences can be seen near the K or L edges for some of the compounds. A good agreement is observed between EPDL97 and XCOM for all compounds except the low energies region for the coherent coefficients. With some exceptions, most of the data points fall within the ±3% region. The percent differences are summarised in table 2 and 3 for the different materials investigated.

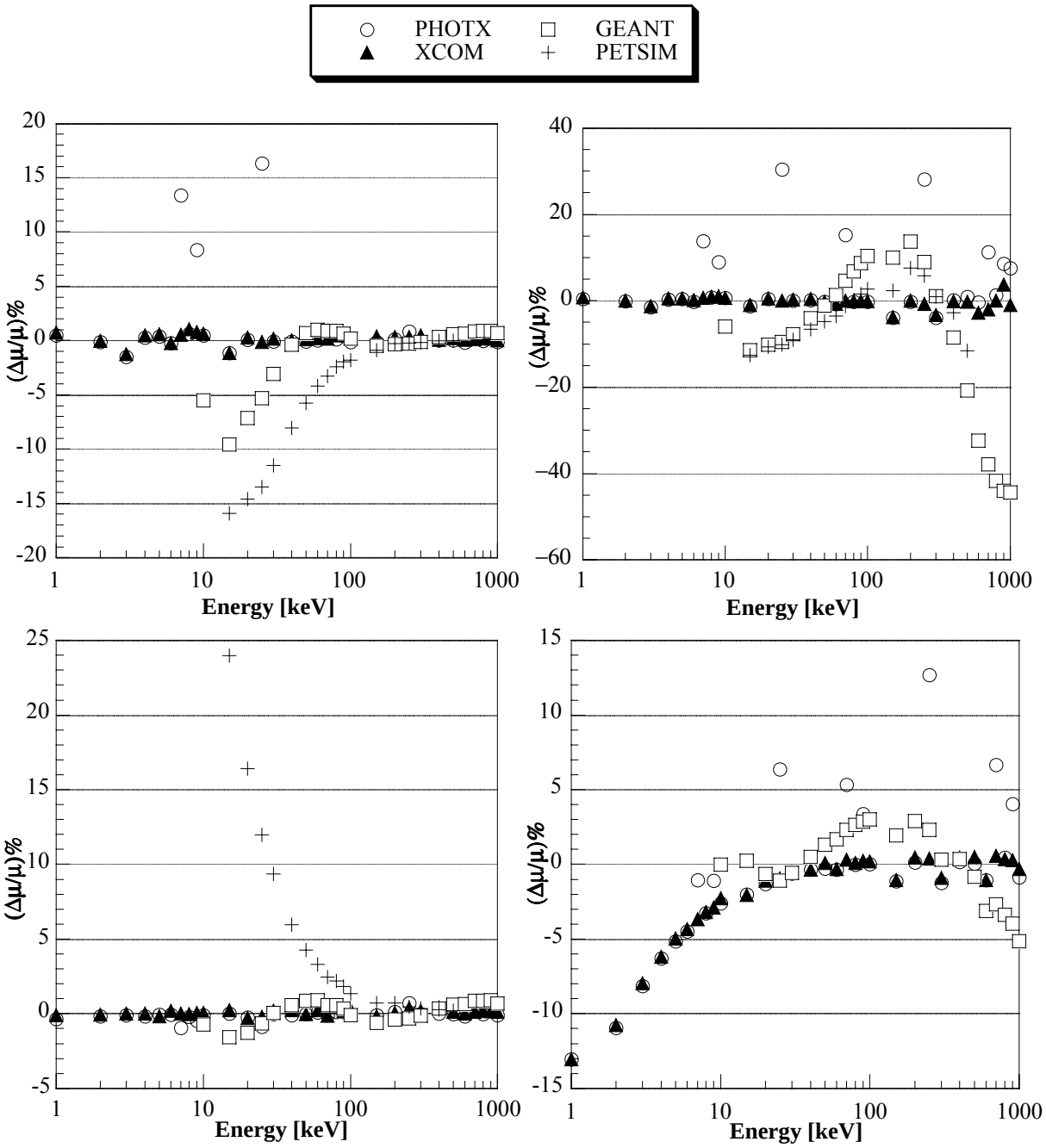


**Figure 3.** Comparisons (percent differences) between the different libraries and the EPDL97 database for water ($H_2O$). The coefficients shown are: total (top left), photoelectric (top right), incoherent (bottom left) and coherent (bottom right). The comparisons were calculated at energies given to the keV resolution between 1 and 1000 keV for both XCOM and PHOTX, between 10 and 1000 keV for GEANT, and between 15 and 511 keV for PETSIM.

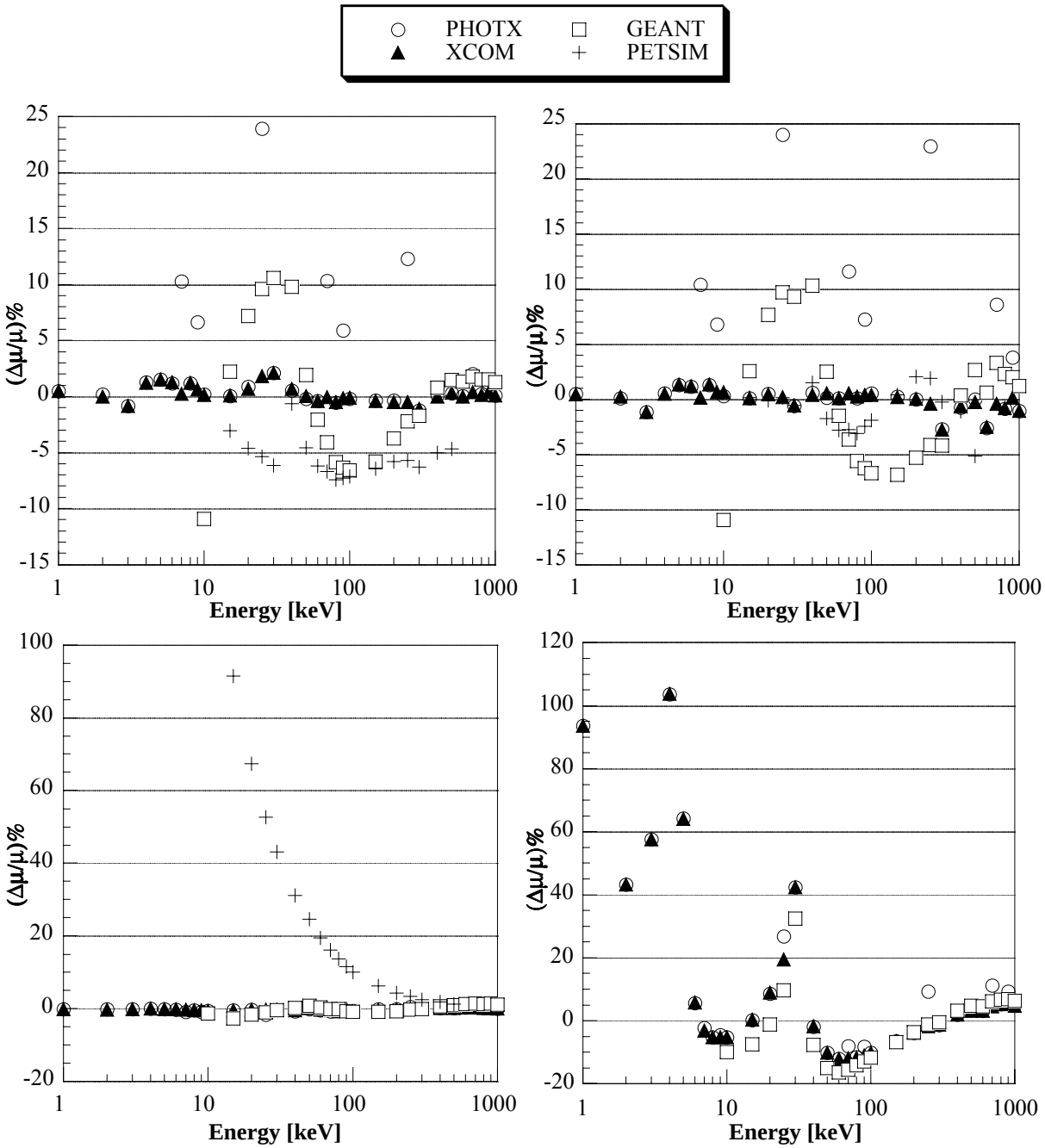


**Figure 4.** Comparisons (percent differences) between the different libraries and the EPDL97 database for sodium iodide (NaI(Tl). The coefficients shown are: total (top left), photoelectric (top right), incoherent (bottom left) and coherent (bottom right). The comparisons were calculated at energies given to the keV resolution between 1 and 1000 keV for both XCOM and PHOTX, between 10 and 1000 keV for GEANT, and between 15 and 511 keV for PETSIM.

**Table 2.** Global estimates of relative differences between PHOTX and XCOM libraries and EPDL97 coefficients. Mean relative errors with standard deviations over the energy range 250 to 511 keV are shown.

| | XCOM | | | | PHOTX | | | |
|---|---|---|---|---|---|---|---|---|
| | Total | Photoelectric | Incoherent | Coherent | Total | Photoelectric | Incoherent | Coherent |
| Water | 0.24 ± 0.17 | 1.74 ± 0.78 | 0.24 ± 0.18 | 0.40 ± 0.29 | 0.28 ± 0.22 | 7.67 ± 7.29 | 0.26 ± 0.20 | 3.74 ± 3.20 |
| Bone (Cort) | 0.21 ± 0.16 | 1.40 ± 0.58 | 0.20 ± 0.15 | 0.29 ± 0.17 | 0.59 ± 0.29 | 7.53 ± 7.28 | 0.50 ± 0.19 | 4.0 ± 3.08 |
| Lung (Infl) | 0.23 ± 0.18 | 1.72 ± 0.74 | 0.23 ± 0.18 | 0.42 ± 0.29 | 0.63 ± 0.22 | 7.09 ± 7.37 | 0.61 ± 0.20 | 4.07 ± 3.09 |
| Brain tissue | 0.23 ± 0.17 | 4.28 ± 0.69 | 0.24 ± 0.18 | 0.75 ± 0.36 | 0.64 ± 0.22 | 7.73 ± 7.58 | 0.61 ± 0.20 | 3.87 ± 3.22 |
| Air | 0.29 ± 0.21 | 1.58 ± 0.68 | 0.29 ± 0.21 | 0.33 ± 0.24 | 0.60 ± 0.38 | 7.83 ± 7.66 | 0.73 ± 0.31 | 4.15 ± 3.22 |
| NaI(Tl) | 0.44 ± 0.39 | 1.44 ± 0.70 | 0.12 ± 0.07 | 1.58 ± 0.79 | 2.83 ± 3.07 | 6.37 ± 6.11 | 0.32 ± 0.12 | 4.85 ± 2.06 |
| BGO | 0.73 ± 0.45 | 1.30 ± 0.56 | 0.11 ± 0.08 | 2.25 ± 1.32 | 3.52 ± 3.46 | 5.01 ± 4.58 | 0.22 ± 0.11 | 3.83 ± 1.50 |
| $BaF_2$ | 0.42 ± 0.35 | 1.33 ± 0.61 | 0.12 ± 0.06 | 1.56 ± 0.89 | 2.92 ± 3.15 | 6.32 ± 6.03 | 0.32 ± 0.12 | 4.78 ± 1.94 |
| LSO:Ce | 0.50 ± 0.32 | 0.91 ± 0.44 | 0.13 ± 0.08 | 1.98 ± 1.16 | 5.14 ± 3.92 | 7.68 ± 5.85 | 1.54 ± 0.13 | 5.50 ± 1.90 |
| LuAP:Ce | 0.43 ± 0.29 | 0.83 ± 0.42 | 0.09 ± 0.06 | 1.98 ± 1.16 | 4.96 ± 3.85 | 7.69 ± 5.89 | 1.44 ± 0.12 | 5.45 ± 1.89 |

**Table 3.** Global estimates of relative differences between GEANT and PETSIM parametrizations and EPDL97 coefficients. Mean relative errors with standard deviations over the energy range 250 to 511 keV are shown.

| | GEANT | | | | PETSIM | | | |
|---|---|---|---|---|---|---|---|---|
| | Total | Photoelectric | Incoherent | Coherent | Total | Photoelectric | Incoherent | Coherent |
| Water | 0.30 ± 0.13 | 9.61 ± 6.82 | 0.31 ± 0.13 | 0.85 ± 0.44 | 0.11 ± 0.08 | 5.12 ± 3.79 | 0.29 ± 0.11 | - |
| Bone (Cort) | 0.32 ± 0.16 | 3.10 ± 1.57 | 0.33 ± 0.16 | 1.65 ± 0.80 | 0.42 ± 0.17 | 4.21 ± 3.15 | 0.50 ± 0.14 | - |
| Lung (Infl) | 0.39 ± 0.20 | 8.37 ± 5.93 | 0.39 ± 0.20 | 0.86 ± 0.48 | 0.25 ± 0.08 | 4.71 ± 2.75 | 0.14 ± 0.11 | - |
| Brain tissue | 0.39 ± 0.20 | 8.18 ± 5.81 | 0.40 ± 0.20 | 0.86 ± 0.49 | 0.73 ± 0.08 | 4.91 ± 3.34 | 0.34 ± 0.11 | - |
| Air | 0.33 ± 0.24 | 9.73 ± 6.90 | 0.33 ± 0.24 | 1.24 ± 0.97 | 0.24 ± 0.16 | 4.87 ± 3.43 | 0.34 ± 0.22 | - |
| NaI(Tl) | 0.98 ± 0.68 | 1.73 ± 1.58 | 0.51 ± 0.33 | 2.36 ± 1.33 | 5.41 ± 0.46 | 2.29 ± 1.99 | 1.96 ± 0.57 | - |
| BGO | 1.01 ± 0.72 | 1.96 ± 1.02 | 1.60 ± 0.46 | 5.03 ± 2.68 | 1.92 ± 0.78 | 1.76 ± 1.31 | 13.94 ± 0.72 | - |
| $BaF_2$ | 0.95 ± 0.71 | 1.75 ± 1.51 | 0.51 ± 0.32 | 3.32 ± 1.77 | 5.03 ± 0.35 | 2.28 ± 1.73 | 2.20 ± 0.55 | - |
| LSO:Ce | 1.33 ± 0.78 | 1.38 ± 0.96 | 1.81 ± 0.47 | 5.09 ± 2.45 | 3.40 ± 0.36 | 1.83 ± 1.42 | 7.46 ± 0.61 | - |
| LuAP:Ce | 1.30 ± 0.76 | 1.38 ± 0.96 | 1.74 ± 0.45 | 5.06 ± 2.43 | 9.24 ± 1.02 | 1.83 ± 1.37 | 5.66 ± 0.50 | - |

## 4. PARALLEL IMPLEMENTATION OF THE SIMULATOR

The *Eidolon* Monte Carlo software was developed to simulate cylindrical 3D positron tomographs.[14] The original code was written in Objective-C and run under the NeXTSTEP object-oriented development environment. Although, the NeXTSTEP environment provided a great development tool allowing to reduce the amount of time necessary for writing applications, the portability issue still remained hard to solve since these applications were tied to machines running NeXTSTEP. Fortunately, the GNU C compiler (gcc) available from the Free Software Foundation comes with an Objective-C compiler and a runtime library since version 2.7.1. This makes it possible to port *Eidolon* on most of the current platforms and operating systems.

Although variance reduction techniques such as forced detection and stratification increase computational efficiency,[1] Monte Carlo modelling is still computationally demanding, and so ways of increasing the speed of simulations are of interest. In photon transport simulation, scalar or serial Monte Carlo codes track the history of one particle at a time, and the total calculation time is the sum of the time consumed in each particle history. Many Monte Carlo applications have characteristics that make them easy to map onto computers having multiple processors. Some of these parallel implementations require little or no interprocessor communication, and are typically easy to code on a parallel computer. Others require frequent communication and synchronisation among processors and in general are more difficult to write and debug. A common way to parallelise Monte Carlo is to put identical "clones" on the various processors; only the random numbers are different. It is therefore important for the sequences on the different processors to be uncorrelated so that each

processor does not end up simulating the same data. In the parallel implementation of *Eidolon*, the random seeds are appropriately defined and distributed to different processors for doing the same calculations. Thus it was possible to achieve a linear scaling of the computing time with the number of processors.[15]

## 5. SHAPE-BASED VERSUS VOXEL-BASED MONTE CARLO SIMULATIONS

Object modelling is fundamental for performing photon and electron transport efficiently by means of a Monte Carlo method. It consists of a description of the geometry and material characteristics for an object.[1] The material characteristics of interest include density and energy-dependent cross-sections. The modelling includes simple geometry (SG), shape-based (SB), and voxel-based (VB) approaches. The three approaches use a piece wise uniform distribution of object characteristics to model an object. With the SG model, an object is composed of a simple combination of primitives such as cylinders and spheres. The SB approach represents the boundaries of shapes by mathematical equations. Regular shapes such as spheres, cylinders, parallelepipeds, etc. have been used to approximate irregularly-shaped regions. The VB approach discretizes an object into tiny cubes (voxels) with uniform characteristics. An object is thus represented by a union of voxels of the same size. As an improvement to the mathematical anthropomorphic phantoms, a new family of phantoms was constructed from CT and MRI data. The human phantoms present advantages towards the location and shape of the organs, in particular the hard bone and bone marrow. A physical brain phantom has also been developed to simulate the activity distributions found in the human brain in the cerebral blood flow and metabolism studies currently employed in PET.[16] The phantom utilises thin layers of Lucite to provide apparent relative concentrations of 4, 1 and 0 for gray matter, white matter and ventricles, respectively, in the brain. A clinically realistic source distribution simulating brain imaging was created in digital format. Zubal[17] developed a typical anthropomorphic VB adult phantom by manual segmentation of CT transverse slices of a living human male performed by medical experts. A computerised 3D volume array modelling all major internal structures of the body was then created. Each voxel of the volume contains an index number designating it as belonging to a given organ or internal structure. These indexes can then be used to assign a value, corresponding to, e.g. density or activity.

The current version of the program is capable of modelling photon transport through media in which the material properties vary in three dimensions. Both SB and VB models are supported within the simulator. A detailed description of the way to specify the source and scattering medium for the SB model is given elsewhere.[18] The advantages of the VB model is to allow some calculations requiring the use of more accurate representations of individuals based on volumetric scans, such as CT, MRI to be made at the expense of the increased computing time. Ray-tracing approaches based on an implementation of Siddon's algorithm are used to compute the length of intersection of each ray with every voxel. By considering pixel boundaries as the intersection of orthogonal sets of equally spaced planes, rather than independently, the computational complexity is greatly reduced. The points of intersection of a line with a set of parallel planes are particularly simple to determine. Once one such point has been found, all the others may be found by recursion. A detailed description of the algorithm may be found elsewhere.[19] Figure 5 shows the Hoffman brain phantom[16] generations in scatter-free conditions and when considering attenuation and scattering within the phantom and the detector blocks, respectively.

## 6. DISCUSSION AND CONCLUSIONS

Monte Carlo modelling has contributed to a better understanding of the physics of photon transport in medical physics. The large number of applications of the Monte Carlo method asserts for its usefulness as a research tool in different areas of nuclear imaging. In the first version of the software, interaction cross-sections and scattering distributions were computed from parametrizations implemented in the GEANT simulation package. It has been shown that different photon cross-section libraries show quite large variations as compared to the most recent EPDL97 nuclear data files. The cross-section values produced by the LLNL are thought to be the most up-to-date and accurate coefficients available, and the LLNL database is now a national and international standard for use in the nuclear industry.[13] Therefore we highly recommend that EPDL97 cross-section data supersedes earlier cross-section libraries used in Monte Carlo codes to simulate medical imaging systems. The library was carefully designed in the form of look-up tables for efficiency in data storage, access, and use by the Monte Carlo software. The mean relative errors for water linear attenuation coefficients in the energy range 250 to 511 keV between XCOM and EPDL97 are (1.74±0.78)%, (0.24±0.18)%, (0.40±0.29)% and (0.24±0.17)% for photoelectric effect, incoherent scattering, coherent scattering and total linear attenuation coefficients, respectively. They are (5.12±3.79)%, (0.29±0.11)% and (0.11±0.08)% between PETSIM and EPDL97 for photoelectric effect, incoherent scattering and total linear attenuation coefficients, respectively.

Together with the optimisation of the computing time performances of the Monte Carlo software, photon transport in 3D PET could be efficiently modelled to better understand scatter correction techniques. The accuracy in correction methods

can thus be evaluated in an unbiased way since systematic errors can be controlled. In implementing *Eidolon* on a parallel architecture, a linear increase in computing speed was achieved with the number of computing nodes.[15] The speed increase due to parallelisation makes Monte Carlo simulation more attractive as a tool for modelling photon transport in 3D PET.

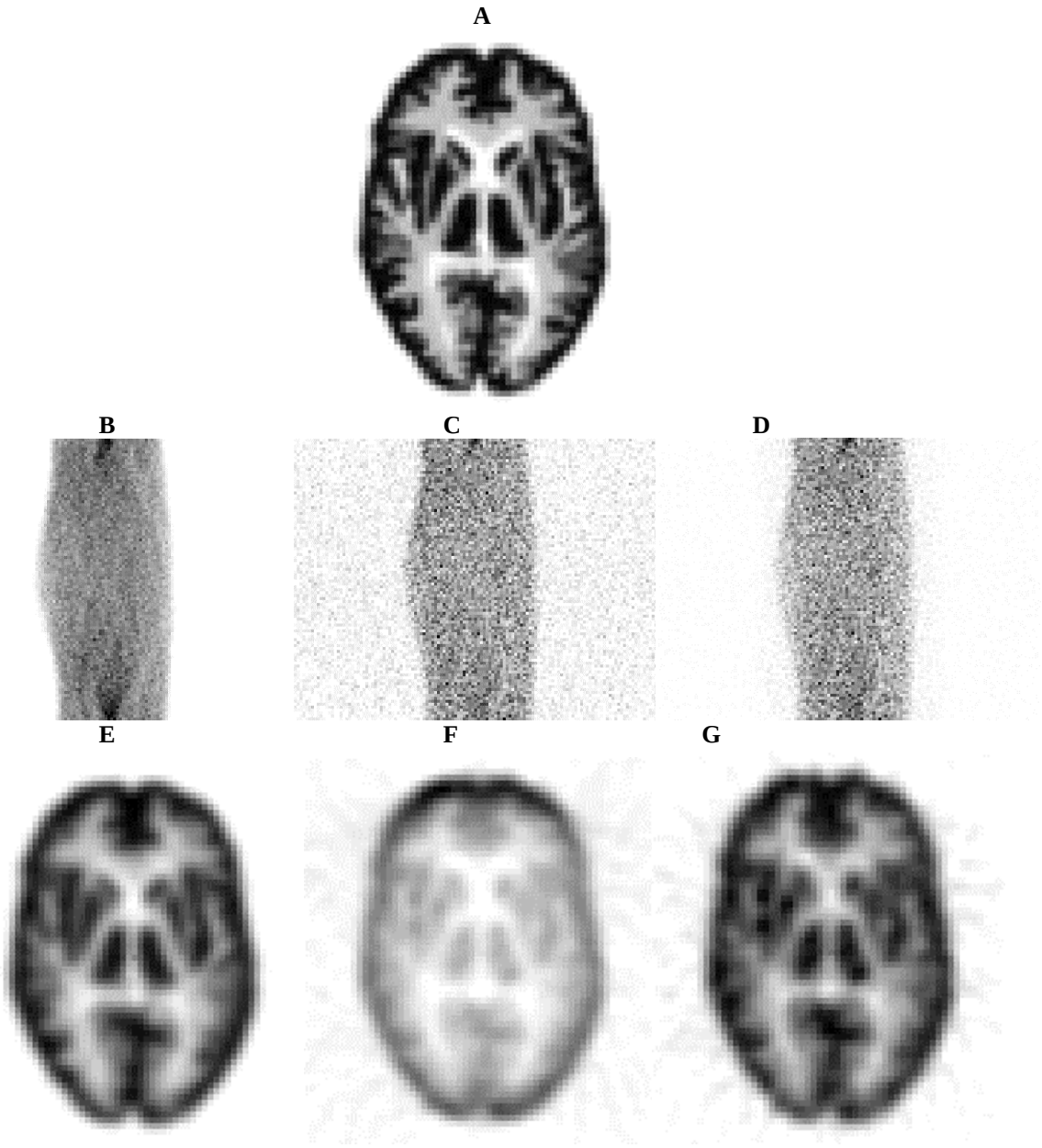


**Figure 5.** Simulation of the Hoffman brain phantom in different imaging situations. The expected image is shown in **A**. **B** and **E** are respectively a sinogram where attenuation and scatter are not simulated, and the corresponding 3D image reconstructed using the reprojection algorithm. **C** and **F** are respectively the same sinogram, but generated with attenuation and scatter simulation, and the corresponding 3D image. **D** and **G** are again the same sinogram generated with attenuation and scatter simulation, and the corresponding 3D image reconstructed this time after applying attenuation corrections to the sinogram data.

## ACKNOWLEDGEMENTS

This work was supported by the Swiss Federal Office for Education and Science under grant 96.193 within the European Esprit LTR project PARAPET (EP23493). The authors gratefully thank their partners within the PARAPET project.

## REFERENCES


1. H. Zaidi, "Relevance of accurate Monte Carlo modeling in nuclear medical imaging," Med. Phys. **26**, pp 574-608, 1999.
2. J. H. Hubbell, "Review of photon interaction cross section data in the medical and biological context," Phys. Med. Biol. **44**, pp 1–22, 1999.
3. D. E. Cullen, J. Hubbell, L. Kissel, "EPDL97: the Evaluated Photon Data Library, '97 Version ," Lawrence Livermore National Laboratory. UCRL-50400, Vol. 6, Rev. 5 (1997).
4. M. J. Berger and J. H. Hubbell, "XCOM: Photon cross sections on a personal computer," NBSIR 87-3597 (1987).
5. D. K. Trubey, M. J. Berger and J. H. Hubbell, "Photon cross sections for ENDF/B-IV," Paper presented at the American Nuclear Society Topical Meeting, Advances in Nuclear Engineering Computation and Radiation Shielding, Santa Fe, New Mexico, (April 9-13, 1989).
6. Brun R, Bruyant F, Maire M, McPherson AC, and Zanarini P. GEANT detector description and simulation tool, CERN Program Library, W5013 (1994).
7. Y. Picard, C. J. Thompson and S. Marrett, "Improving the precision and accuracy of Monte Carlo simulation in positron emission tomography," IEEE Trans Nucl Sci **39**, pp 1111-1116, 1993.
8. C. R. Askew, D. B. Carpenter, J. T. Chalker, et al., "Monte Carlo simulation on transputer arrays," J. Parallel Computing **6**, pp 247-258, 1988.
9. M. F. Smith, C. E. Floyd, R. J. Jaszczak, "A vectorized Monte Carlo code for modeling photon transport in SPECT," Med. Phys. **20**, pp 1121-1127, 1993.
10. R. G. Babb and L. Storc, "Developing a parallel Monte Carlo transport algorithm using large-grain data flow," Parallel Comput. **7**, pp 187-198, 1988.
11. D. R. Kirkby and D. T. Delpy, "Parallel operation of Monte Carlo simulations on a diverse network of computers," Phys. Med. Biol. **42**, pp 1203-1208, 1997.
12. ICRU, "Tissue Substitutes in Radiation Dosimetry and Measurement," Report 44 of the International Commission on Radiation Units and Measurements (Bethesda, MD, 1989).
13. J. M. Boone and A. E. Chavez, "Comparison of x-ray cross sections for diagnostic and therapeutic medical physics," Med. Phys. **23**, pp 1997-2005, 1997.
14. H. Zaidi, A. Herrmann Scheurer and C. Morel, "An object-oriented Monte Carlo simulator for 3D positron tomographs," Comput. Methods Programs Biomed. **58**, pp 133-145, 1999.
15. H. Zaidi, C. Labbé, and C. Morel, "Implementation of an environment for Monte Carlo simulation of fully 3D positron tomography on a high-performance parallel platform," Parallel Computing **24** (9-10), pp 1523-1536, 1998.
16. E. J. Hoffman, P. D. Cutler, W. M. Digby, and J. C. Mazziotta, "3-D phantom to simulate cerebral blood flow and metabolic images for PET," IEEE Trans. Nucl. Sci. **37**, pp 616-620, 1990.
17. G. Zubal, C. R. Harrell, E. O. Smith, Z. Rattner, G. Gindi, B. P. Hoffer, "Computerized 3-Dimensional segmented human anatomy," Med. Phys. **21**, pp 299-302, 1994.
18. H. Zaidi, C. Labbé, and C. Morel, "A Monte Carlo simulator for multi-ring PET scanners", Parapet Project Documentation D2.1, December 1997.
19. Siddon R L, "Fast calculation of the exact radiological path for a three-dimensional CT array," Med. Phys. **12**, pp 252-255, 1985.



† Correspondance email: habib.zaidi@hcuge.ch; WWW: http://dmnu-pet5.hcuge.ch/Habib/home.html